dc transport in perturbed multichannel quantum wires

C. Berthod, F. Gagel, and K. Maschke
Institut de Physique Appliquée, Ecole Polytechnique Fédérale, CH-1015 Lausanne, Switzerland
(Received 27 June 1994)

We investigate the influence of local defects on the dc transport in mesoscopic quantum wires of finite width. Using the Anderson Hamiltonian for the description of the wires, we solve the Schrödinger equation for scattering boundary conditions. The conductance is then calculated within the Landauer approach. We present a detailed study of the defect-induced fluctuations in the conductance spectra, which are of the order of e^2/h. These fluctuations can be related with Fano resonances in the electron transmission spectra, which are due to the coupling between localized defect states and the propagating states of the perfect waveguide. Different kinds of defects are investigated. The case of the double Anderson chain is treated with particular emphasis, since in spite of its simplicity this system possesses all the characteristic features of more complex systems. Our analytical and numerical results reveal the intimate relation between conduction spectra and localized impurity states and provide a basis for the understanding of conductance spectroscopy experiments in mesoscopic systems. The importance of the interaction between localized states and propagating states is also demonstrated by our results for the local current distribution, which becomes strongly inhomogeneous and even vortexlike for Fermi energies near the Fano resonances.

I. INTRODUCTION

During the past twenty years, the great importance of quantum interference effects for the dc transport properties of mesoscopic samples has been well established as well experimentally as theoretically.[1] The basis for our present understanding of the related phenomena has been given by the work of Landauer[2,3] who has related the conductance to the scattering properties of the considered system. The specific merit of his approach is that it reveals the essential difference between elastic and inelastic scattering processes: The latter destroy the phase memory and are responsible for dissipation of energy, whereas the nondissipative and phase conserving elastic scattering processes introduce quantum interference effects due to the *coherent* scattering between defects. This clarification has stimulated many researchers to look for the effects of quantum coherence in dc transport, which have got a great importance with the development of mesoscopic devices. Among the most important consequences of the interference between coherently scattered waves, we mention the localization of electron states in disordered media,[1,2,4] weak localization effects which are due to the constructive interference between coherently backscattered electrons,[1,5] coherent magnetotransport,[1,6,7] and the existence of universal conductance fluctuations in disordered media, which in spite of being sample specific are always of the order of e^2/h.[1,8–10] While the above-mentioned effects are by now well understood in principle, much remains to be done to explore the exciting possibilities in the field of mesoscopic transport.

In the present work, we concentrate on the coherent transport in multichannel quantum wires in presence of defects. Quantum wires are apparently the simplest systems which can be discussed in the field of mesoscopic transport and have already been discussed by many authors.[1,11–14] One may, therefore, wonder whether they are still of actual interest. Having a closer look, one recognizes, however, that any mesoscopic device can be described as a multichannel quantum wire which is tailored by a special distribution of "defects," and that therefore multichannel quantum wires with defects can be considered as the most general mesoscopic physical systems. Historically, the understanding of the principles of quantum interference phenomena has been obtained by considering single-channel systems which are representative for one-dimensional (1D) systems, and many authors have contributed to this.[1,2,15–17] In this case, the conductance oscillations in the mesoscopic regime can be described in terms of Fabry-Pérot interferences between multiple scattered monochromatic electron waves near the Fermi energy E_F with Fermi-wave vector k_F. During the past decade, it has been demonstrated both experimentally and theoretically that multichannel systems present a lot of interesting interference phenomena which cannot be explained within a 1D description. These features can be attributed to the presence of interchannel coupling. It is thus worthwhile to develop a general picture which allows us to understand the specific effects of interchannel coupling. In this spirit, we will, in the following, analyze the behavior of rather simple multichannel systems, which will allow us to develop insight into this fascinating world of interference phenomena in mesoscopic systems. The present study was stimulated by the recent work of Tekman and Bagwell,[18] who showed that defects in quantum wires lead to Fano resonances in the electron transmission spectra. These resonances, which result from the coherent coupling between localized impurity states and the continuum of propagating states,

0163-1829/94/50(24)/18299(13)/$06.00

have been discussed, also, by other authors.[19,20]

Our theoretical approach, which differs in several respects from previous studies, is presented in Sec. II. The perturbed wire is represented by an Anderson Hamiltonian. The Schrödinger equation for scattering boundary conditions leads to an inhomogeneous system of linear equations which defines the scattering properties of the system. The conductance of the perturbed quantum wire as well as the local current distribution are then calculated using the Landauer approach. In Sec. III, we present our numerical results for a variety of systems. For reasons of simplicity, we restrict our discussion to 2D wires with rather simple defect distributions, which is sufficient for our present purpose. The case of the double Anderson chain is treated with particular attention, since all the characteristic features of more complex systems are already present and can be discussed in a transparent manner.

II. THEORETICAL APPROACH

A. General case

We consider the quantum wire represented in Fig. 1. It consists of a perturbed region M and two identical perfect waveguides attached to both sides. At both ends the waveguides are connected to electron reservoirs with slightly different chemical potentials μ_{left} and μ_{right}. In order to avoid unnecessary complications, we assume that the energetic distribution of the electrons is given by the Fermi distribution function at zero temperature. The waveguides are considered to be semi-infinite. This ensures that only electrons which are injected from the reservoirs in *propagating* modes of the waveguides can contribute to the current, all others are reflected back into the reservoirs. The dc conductance can then be expressed in terms of transmission probabilities of electrons near the Fermi level, i.e., the dc transport properties are expressed in terms of the scattering properties of the system.[2,3]

The Hamiltonian of the considered quantum wire may be split into two parts,

$$H = H_0 + H_1, \tag{1}$$

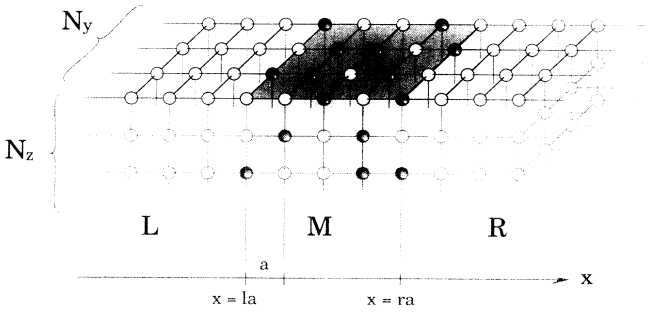

FIG. 1. Quantum wire with defects in the Anderson model. L and R denote the regions of the semi-infinite waveguides, which are connected to electron reservoirs with different chemical potentials. The region M contains the defects.

where H_0 represents the perfect wire without defects, and H_1 describes the defects. The solution of the Schrödinger equation for scattering boundary conditions is expressed in terms of the incoming wave function $|\psi_{\text{in}}\rangle$ and the scattered wave function $|\psi_{\text{scatt}}\rangle$, i.e.,

$$|\psi\rangle = |\psi_{\text{in}}\rangle + |\psi_{\text{scatt}}\rangle. \tag{2}$$

From the Schrödinger equation, we obtain

$$(H - E)|\psi_{\text{scatt}}\rangle = (E - H)|\psi_{\text{in}}\rangle, \tag{3}$$

which relates the scattered wave $|\psi_{\text{scatt}}\rangle$ to the incoming wave $|\psi_{\text{in}}\rangle$. In the following, we describe the system by an Anderson Hamiltonian, which is expressed in the orthonormal Wannier basis $|\mathbf{n}\rangle = |n_x, n_y, n_z\rangle$. Here, the vectors $(n_x, n_y, n_z)a$ run over the lattice points of a cubic lattice, i.e., for a quantum wire along the x axis and with lateral dimensions $N_y a$ and $N_z a$, we have

$$\begin{aligned} n_x &= -\infty, \ldots, -1, 0, 1, \ldots, \infty, \\ n_y &= 1, \ldots, N_y, \\ n_z &= 1, \ldots, N_z. \end{aligned}$$

In this basis, the matrix elements of H_0 and H_1 become

$$\langle \mathbf{n}|H_0|\mathbf{n}'\rangle = V(\Delta^{(x)}_{\mathbf{nn}'} + \delta_{n_z n'_z}\Delta^{(yz)}_{\mathbf{nn}'}) + \epsilon\delta_{\mathbf{nn}'}, \tag{4}$$

$$\langle \mathbf{n}|H_1|\mathbf{n}'\rangle = \epsilon_{\mathbf{n}}\delta_{\mathbf{nn}'}, \tag{5}$$

with

$$\Delta^{(x)}_{\mathbf{nn}'} = (\delta_{n_x n'_x+1} + \delta_{n_x n'_x-1})\delta_{n_y n'_y}\delta_{n_z n'_z},$$

$$\Delta^{(yz)}_{\mathbf{nn}'} = \begin{cases} 1 & \text{if } \mathbf{n}, \mathbf{n}' \text{ are nearest neighbors in the } (yz) \text{ plane} \\ 0 & \text{otherwise.} \end{cases}$$

The first term in Eq. (4) describes the coupling between nearest neighbors. In the following, we choose the origin of the energy such that $\epsilon = 0$. The defects are described by the potential parameters $\epsilon_{\mathbf{n}}$ in Eq. (5). Since H_0 is separable with respect to the coordinates x and y,z, we may write $H_0 = H_0^{(x)} + H_0^{(yz)}$, and the eigenfunctions of H_0 to the energy E can be written as[21]

$$\begin{aligned} |\nu, E\rangle &= \sum_{n_x, n_y, n_z} \kappa_\nu^{n_x} \phi^\nu_{n_y n_z} |n_x, n_y, n_z\rangle \\ &\equiv \sum_{n_x} |n_x, \nu, E\rangle. \end{aligned} \tag{6}$$

In the following, we use the normalizations

$$\sum_{n_y,n_z} \phi^{\nu}_{n_y n_z} \phi^{\nu'}_{n_y n_z} = \delta_{\nu\nu'},$$
$$\langle n_x, \nu, E | n'_x, \nu', E \rangle = |\kappa_\nu|^{2n_x} \delta_{n_x n'_x} \delta_{\nu\nu'}.$$

The index ν labels the $N = N_y N_z$ modes which correspond to the eigenstates of $H_0^{(yz)}$. The factor κ_ν describes the behavior of the eigenmodes ν along the waveguide: For evanescent states, we have $|\kappa_\nu| < 1$; propagating modes may also be characterized by the corresponding wave vector q_ν with $\kappa_\nu = \exp(iq_\nu a)$. The ket vectors $|n_x, \nu, E\rangle$ give the projection of the eigenstate $|\nu, E\rangle$ on a plane corresponding to a particular n_x. The Schrödinger equation for the unperturbed waveguide becomes

$$V\left(\kappa_\nu \phi^{\nu}_{n_y n_z} + \frac{1}{\kappa_\nu}\phi^{\nu}_{n_y n_z} + \sum_{n'_y, n'_z} \phi^{\nu}_{n'_y n'_z} \Delta^{(yz)}_{\mathbf{n}\mathbf{n}'}\right) = E \phi^{\nu}_{n_y n_z}. \tag{7}$$

With the definitions

$$E^{(x)}_\nu = V\left(\kappa_\nu + \frac{1}{\kappa_\nu}\right), \tag{8}$$

$$E^{(yz)}_\nu \phi^{\nu}_{n_y n_z} = V \sum_{n'_y, n'_z} \phi^{\nu}_{n'_y n'_z} \Delta^{(yz)}_{\mathbf{n}\mathbf{n}'}, \tag{9}$$

we obtain for the energy

$$E = E^{(x)}_\nu + E^{(yz)}_\nu. \tag{10}$$

The wave functions $|\nu, E\rangle$ vanish in the region outside the wire. We, therefore, solve Eq. (9) with the boundary conditions $\phi^{\nu}_{0,n_z} = \phi^{\nu}_{n_y,0} = \phi^{\nu}_{N_y+1,n_z} = \phi^{\nu}_{n_y,N_z+1} \equiv 0$. It is evident from the above equations that κ_ν and $1/\kappa_\nu$ are interchangeable: In the following, we assume $|\kappa_\nu| \leq 1$ in Eq. (6), which corresponds to propagating states or to evanescent states in the forward direction. States scattered in the backward direction are then obtained by replacing $\kappa_\nu^{n_x}$ by $\kappa_\nu^{-n_x}$.

We now consider a wave incoming from the left side in channel $\bar{\nu}$. Denoting the region of the waveguide to the left (right) of the perturbed region by L (R), and the defect region by M (see Fig. 1), we obtain for the incoming wave

$$|\psi_{\rm in}\rangle \equiv |\bar{\nu}\rangle = \sum_{n'_x \in L} \sum_{\nu'=1}^{N} \delta_{\bar{\nu}\nu'} |n'_x, \nu', E\rangle. \tag{11}$$

The scattered wave is projected on L, M, and R, i.e., we write

$$|\psi_{\rm scatt}\rangle = |\psi^{(L)}_{\bar{\nu}}\rangle + |\psi^{(M)}_{\bar{\nu}}\rangle + |\psi^{(R)}_{\bar{\nu}}\rangle, \tag{12}$$

with

$$|\psi^{(L)}_{\bar{\nu}}\rangle = \sum_{n'_x \in L} \sum_{\nu'=1}^{N} \xi_{\nu'\bar{\nu}} \kappa_{\nu'}^{-2n'_x} |n'_x, \nu', E\rangle,$$
$$|\psi^{(M)}_{\bar{\nu}}\rangle = \sum_{n'_x \in M} \sum_{\nu'=1}^{N} \psi^{\bar{\nu}}_{n'_x \nu'} |n'_x, \nu', E\rangle, \tag{13}$$
$$|\psi^{(R)}_{\bar{\nu}}\rangle = \sum_{n'_x \in R} \sum_{\nu'=1}^{N} \xi_{\nu'+N,\bar{\nu}} |n'_x, \nu', E\rangle.$$

In the following, we assume that the perturbed region extends over the layers between l and r (see Fig. 1). With this choice the layer indices n_x, which define the subspaces L, M, and R, are given by

$$n^L_x = \{-\infty, \ldots, l-1\},$$
$$n^M_x = \{l, \ldots, r\},$$
$$n^R_x = \{r+1, \ldots, \infty\}.$$

The Schrödinger equation Eq. (3) can now be solved in the representation of the eigenstates of the waveguide, Eq. (6). We obtain (see Appendix A)

$$\begin{pmatrix}
-\mathcal{K}^{-2l+1} & \mathcal{K} & \mathbf{0} & \ldots & \ldots & \ldots & \ldots & \mathbf{0} \\
\mathcal{K}^{-2l+1} & \mathcal{M}^{(l)} & \mathcal{K} & \ddots & & & & \vdots \\
\mathbf{0} & \mathcal{K}^{-1} & \mathcal{M}^{(l+1)} & \ddots & \ddots & & & \vdots \\
\vdots & \ddots & \ddots & \ddots & \ddots & \ddots & & \vdots \\
\vdots & & \ddots & \ddots & \ddots & \ddots & \ddots & \vdots \\
\vdots & & & \ddots & \ddots & \mathcal{M}^{(r-1)} & \mathcal{K} & \mathbf{0} \\
\vdots & & & & \ddots & \mathcal{K}^{-1} & \mathcal{M}^{(r)} & \mathcal{K} \\
\mathbf{0} & \ldots & \ldots & \ldots & \ldots & \mathbf{0} & \mathcal{K}^{-1} & -\mathcal{K}^{-1}
\end{pmatrix}
\begin{pmatrix}
\mathbf{X}^{(L)} \\ \Psi^{(l)} \\ \Psi^{(l+1)} \\ \vdots \\ \vdots \\ \Psi^{(r-1)} \\ \Psi^{(r)} \\ \mathbf{X}^{(R)}
\end{pmatrix}
=
\begin{pmatrix}
\mathcal{K} \\ -\mathcal{K}^{-1} \\ \mathbf{0} \\ \vdots \\ \vdots \\ \mathbf{0} \\ \mathbf{0} \\ \mathbf{0}
\end{pmatrix}. \tag{14}$$

$\mathbf{0}$ is the $N \times N$ null matrix. The $N \times N$ matrices $\mathbf{X}^{(L)}$, $\mathbf{X}^{(R)}$, $\Psi^{(n_x)}$, $\mathcal{K}$, and $\mathcal{M}^{(n_x)}$ are defined by

$$\mathbf{X}^{(L)}_{\nu\nu'} = \xi_{\nu\nu'},$$
$$\mathbf{X}^{(R)}_{\nu\nu'} = \xi_{\nu+N,\nu'},$$
$$\Psi^{(n_x)}_{\nu\nu'} = \psi^{\nu'}_{n_x \nu},$$
$$\mathcal{K}_{\nu\nu'} = \kappa_\nu \delta_{\nu\nu'},$$
$$\mathcal{M}^{(n_x)} = \mathcal{W}^{(n_x)} - \mathcal{K} - \mathcal{K}^{-1}, \tag{15}$$

with

$$\mathcal{W}^{(n_x)}_{\nu\nu'} = \left(\frac{\kappa^*_\nu \kappa_{\nu'}}{|\kappa_\nu|^2}\right)^{n_x} \sum_{n_y, n_z} \phi^{\nu}_{n_y n_z} \phi^{\nu'}_{n_y n_z} \frac{\epsilon_{\mathbf{n}}}{V}. \tag{16}$$

We note that the block matrix in Eq. (14) depends on the choice of the origin. The last column is independent of l and r, reflecting the fact that the transmitted waves $\mathbf{X}^{(R)}$ do not depend on the position of the perturbed region.

From the wave functions, we may also calculate the

local current distribution within the sample. This is best done by expressing the solution of Eq. (14) for an incoming wave in channel $\bar{\nu}$ in the Wannier representation:

$$|\psi_{\bar{\nu}}\rangle = \sum_{n_x,n_y,n_z} \psi^{\bar{\nu}}_{n_x n_y n_z} |n_x, n_y, n_z\rangle.$$

With the position operator $\hat{x}$,

$$\hat{x} = a \sum_{\mathbf{n}} \mathbf{n}|\mathbf{n}\rangle\langle\mathbf{n}|$$

and the Hamiltonian H [Eqs. (4) and (5)], we calculate the velocity operator $\hat{v}$ from

$$\hat{v} = \frac{i}{\hbar}(H\hat{x} - \hat{x}H),$$

which defines the current operator $\hat{j} = -e\hat{v}$. We then obtain, for the respective contribution of $|\psi_{\bar{\nu}}\rangle$ to the local current,

$$\mathbf{j}(\psi_{\bar{\nu}}; n_x, n_y, n_z) = \frac{Vae}{\hbar} \begin{pmatrix} \mathrm{Im}\left[\psi^{\bar{\nu}*}_{n_x,n_y,n_z}\left(\psi^{\bar{\nu}}_{n_x+1,n_y,n_z} - \psi^{\bar{\nu}}_{n_x-1,n_y,n_z}\right)\right] \\ \mathrm{Im}\left[\psi^{\bar{\nu}*}_{n_x,n_y,n_z}\left(\psi^{\bar{\nu}}_{n_x,n_y+1,n_z} - \psi^{\bar{\nu}}_{n_x,n_y-1,n_z}\right)\right] \\ \mathrm{Im}\left[\psi^{\bar{\nu}*}_{n_x,n_y,n_z}\left(\psi^{\bar{\nu}}_{n_x,n_y,n_z+1} - \psi^{\bar{\nu}}_{n_x,n_y,n_z-1}\right)\right] \end{pmatrix}.$$

After summation over all propagating channels $\bar{\nu}$ and integrating over the energy window defined by $\Delta E = \mu_{\mathrm{left}} - \mu_{\mathrm{right}}$, we get for the local current

$$\mathbf{J}(n_x, n_y, n_z) = \frac{\Delta E}{2} \sum_{\bar{\nu}} g_{\bar{\nu}}(E)\, \mathbf{j}(\psi_{\bar{\nu}}; n_x, n_y, n_z), \quad (17)$$

where $g_\nu(E)$ is the one-dimensional density of states of channel ν. Applying this relation to a perfect waveguide, one obtains the well-known result for the conductance

$$G = N_c \frac{2e^2}{h}, \quad (18)$$

where N_c is the number of propagating channels at the considered Fermi energy E.

In the Landauer approach the dc conductance is expressed in terms of the transmission coefficients which are given by the elements of the scattering matrix $\mathcal{S}$,

$$s_{\nu\bar{\nu}} = \sqrt{\frac{v_{g,\nu}}{v_{g,\bar{\nu}}}}\, \xi_{\nu\bar{\nu}}, \quad (19)$$

where $v_{g,\bar{\nu}}$ and $v_{g,\nu}$ are the group velocities in the incoming and outgoing channels $\bar{\nu}$ and ν, which are zero for evanescent modes. The two-terminal conductance is then obtained[22] by summing over the transmission probabilities from left channels $\bar{\nu}$ to right channels $\nu + N$:

$$G = \frac{2e^2}{h} \sum_{\bar{\nu},\nu} |s_{\nu+N,\bar{\nu}}|^2. \quad (20)$$

It will, therefore, be useful for our later discussion, to eliminate the unknowns $\mathbf{X}^{(L)}$ and $\Psi^{(n_x)}$ $(n_x = l, \ldots, r)$ in Eq. (14), which do not enter Eq. (20). This can be done with the help of transfer matrices, which are defined by

$$\Psi^{(r-i)} = \mathcal{T}^{(i)} \mathbf{X}^{(R)}, \qquad i = 0, \ldots, r-l. \quad (21)$$

We show in Appendix B that the matrices $\mathcal{T}^{(i)}$ can be obtained from the recursive relation

$$\mathcal{T}^{(i)} = \mathbf{1} - \sum_{j=1}^{i} \mathcal{Z}^{(j)} \mathcal{W}^{(r-i+j)} \mathcal{T}^{(i-j)}, \quad (22)$$

where $\mathbf{1}$ is the $N \times N$ identity matrix, and

$$\mathcal{Z}^{(j)}_{\nu\nu'} = \frac{\kappa_\nu^{2j} - 1}{\kappa_\nu - \kappa_\nu^{-1}} \delta_{\nu\nu'}. \quad (23)$$

The transfer matrices can now be used to write the solution of Eq. (14) in the perturbed region in terms of $\mathbf{X}^{(R)}$. In this way, we obtain (see Appendix C)

$$\left[\left(\mathcal{K} - \mathcal{K}^{-1}\right) + \mathcal{U}\right] \mathbf{X}^{(R)} = \mathcal{K} - \mathcal{K}^{-1}, \quad (24)$$

with the interaction matrix $\mathcal{U}$,

$$\mathcal{U} = \sum_{n_x=l}^{r} \mathcal{W}^{(n_x)} \mathcal{T}^{(r-n_x)}. \quad (25)$$

The above inhomogeneous system Eq. (24) was obtained for scattering boundary conditions, and the inhomogeneity accounts for the incoming waves [see also Eq. (3)]. For purposes of our later discussion, we note that the respective homogeneous equation,

$$\left[\left(\mathcal{K} - \mathcal{K}^{-1}\right) + \mathcal{U}\right] \mathbf{Y} = 0, \quad (26)$$

describes the defect-induced bound states, which are found when the direct interaction of the localized states with the degenerate continuum states is neglected. In order to see this, we first set the off-diagonal matrix elements in Eq. (26) equal to zero. This leaves us with the equations

$$\left[\left(\mathcal{K} - \mathcal{K}^{-1}\right) + \mathcal{U}\right]_{\nu\nu} = 0. \quad (27)$$

It is easy to see that these equations yield the eigenvalues of the impurity states associated with the one-dimensional bands ν in absence of interband coupling. Including the off-diagonal elements of the interband interaction $\mathcal{U}$ but still neglecting the direct interaction of the defects with the continuum states, we obtain Eq. (26), which, thus, describes the reference system of interacting localized defect states. With this in mind, it follows immediately from Eqs. (24) and (26), that the transmission coefficients $s_{\bar{\nu}+N,\bar{\nu}}$ vanish at *exactly* the eigenenergies of the system of $N - 1$ interacting defect levels, which is

obtained from Eq. (26) after removing the $\bar{\nu}$th column and $\bar{\nu}$th row of the matrix $\left(\mathcal{K}-\mathcal{K}^{-1}\right)+\mathcal{U}$.

The interaction matrix Eq. (25) is responsible for the defect-induced interchannel coupling, and will, therefore, be the central quantity for our discussion of the influence of defects on the dc conductance. For the case of a single defect layer at position $n_x = l$, we obtain from Eqs. (25) and (22) (with $r = l$)

$$\mathcal{U}^{\mathrm{sl}} = \mathcal{W}^{(l)}. \tag{28}$$

For a system with two defect layers at positions l and r, we have $\mathcal{W}^{(l+1)} = \cdots = \mathcal{W}^{(r-1)} = \mathbf{0}$, and we get

$$\begin{aligned}\mathcal{U}^{\mathrm{dl}} &= \mathcal{W}^{(l)}\mathcal{T}^{(r-l)} + \mathcal{W}^{(r)}\mathcal{T}^{(0)} \\ &= \mathcal{W}^{(l)} + \mathcal{W}^{(r)} - \mathcal{W}^{(l)}\mathcal{Z}^{(r-l)}\mathcal{W}^{(r)}.\end{aligned} \tag{29}$$

We note that for a single defect plane at $l = 0$, the interaction matrix $\mathcal{U}^{\mathrm{sl}}$ becomes independent of the energy. Moreover, since the position of the defect layer has no influence on the resulting transmission coefficients, it follows that the energy dependence of $\mathcal{U}^{\mathrm{sl}}$, which is found putting the defect layer at position $l \neq 0$ [see Eq. (16)], is nonessential. The situation is different for more than one perturbing layer: Already for two defect layers the energy dependence of $\mathcal{U}^{\mathrm{dl}}$, which is introduced by $\mathcal{Z}^{(r-l)}$ in Eq. (29), cannot be eliminated by changing the origin. It will be shown in Sec. III, that this leads to a qualitatively different behavior of the transmission coefficients and of the dc conductance.

B. Application to the double Anderson chain

As mentioned in the beginning, the double Anderson chain is of particular interest for our study. In this case, we have $N_y = 2$ and $N_z = 1$. In the following, we will suppress the z coordinate and use a two-dimensional notation. The two modes of the perfect waveguide are either symmetric or antisymmetric, and will be denoted in the following by the indices s and a, respectively. The solution of Eq. (9) is then

$$\begin{aligned}\phi_1^s &= \phi_2^s = \phi_1^a = -\phi_2^a = \frac{1}{\sqrt{2}}, \\ E_s^{(y)} &= -E_a^{(y)} = V.\end{aligned}$$

It is convenient to characterize the perturbing potential at a given position n_x by its symmetric part σ_{n_x} and its antisymmetric part α_{n_x}, with

$$\begin{aligned}\sigma_{n_x} &= \frac{\epsilon_{n_x,1} + \epsilon_{n_x,2}}{2V}, \\ \alpha_{n_x} &= \frac{\epsilon_{n_x,2} - \epsilon_{n_x,1}}{2V}.\end{aligned} \tag{30}$$

The dispersion of the propagating modes obtained from Eq. (8) is $2V\cos qa$. The resulting band structure for the two eigenmodes is shown in Fig. 2.

Equation (20) gives the conductance G in terms of the transmission coefficients. For Fermi energies below the minimum $E_a^{\min}$ of the antisymmetric band (see Fig. 2), G is defined by the transmission coefficient s_{31}. The latter will be denoted t_{ss} in the following, since it involves only the left and right symmetric modes. We obtain from Eq. (24)

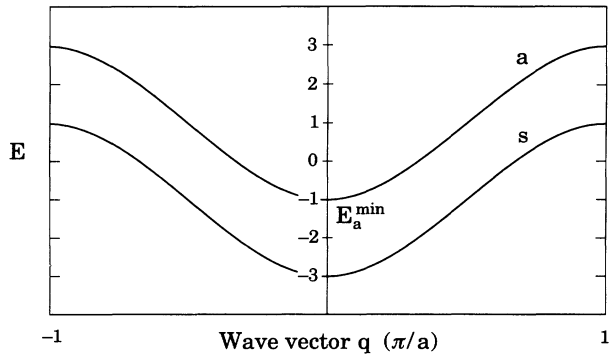

FIG. 2. Band structure of the double Anderson chain for $V = -1$.

$$t_{ss} = \frac{\kappa_s - \kappa_s^{-1}}{\kappa_s - \kappa_s^{-1} + \mathcal{U}_{\mathrm{eff}}}, \tag{31}$$

with

$$\mathcal{U}_{\mathrm{eff}} = \mathcal{U}_{ss} - \frac{\mathcal{U}_{sa}\mathcal{U}_{as}}{\kappa_a - \kappa_a^{-1} + \mathcal{U}_{aa}}. \tag{32}$$

For a single defect at position n_x, this simplifies to

$$\mathcal{U}_{\mathrm{eff}}^{\mathrm{sl}} = \sigma_{n_x} - \frac{\alpha_{n_x}^2}{\kappa_a - \kappa_a^{-1} + \sigma_{n_x}}. \tag{33}$$

In agreement with our previous general discussion, we see that $\mathcal{U}_{\mathrm{eff}}$ diverges at the energy of the impurity level associated with the antisymmetric band, which is given by the condition $\kappa_a - \kappa_a^{-1} + \mathcal{U}_{aa} = 0$, and, therefore, the transmission coefficient t_{ss} vanishes at this energy [see Eq. (31)]. It is interesting to note that Eq. (31) has the same form as the transmission probability for a single point defect in a one-dimensional Anderson chain, with $\mathcal{U}_{\mathrm{eff}}$ equal to ϵ_n/V.

III. NUMERICAL RESULTS

In the following discussion, we use the scales $V = -1$ and $a = 1$ for energies and lengths, respectively. Figure 3 shows our numerical results for the conductance of a two-dimensional double quantum well with rough interfaces. This spectrum is representative and illustrates the typical behavior for a perturbed quantum wire. For reasons of simplicity the width of the quantum wire ($N_y = 6$) is chosen rather small. The results are qualitatively the same for larger widths as well as for 3D quantum wires, the only difference being that the density of the oscillations in the conductance spectrum increases with the number of conducting channels and the graphical resolution becomes more difficult. The geometrical parameters, which specify the considered double well as well as the local

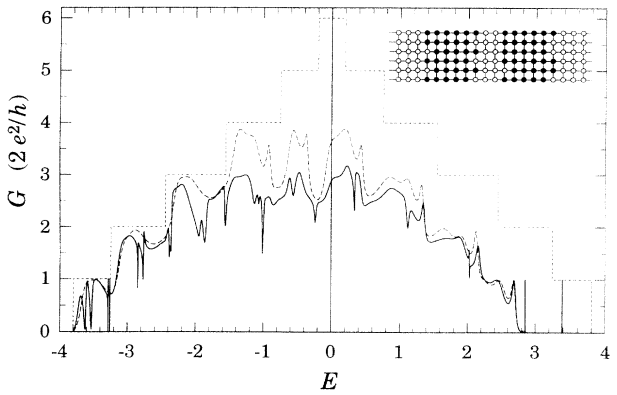

FIG. 3. Conductance for a two-dimensional double well vs the Fermi energy. The vertical width of the quantum wire is $N_y = 6$. The interfaces between waveguides and quantum-well regions are disordered. The actual distribution of site energies in the Anderson Hamiltonian is given in the inset, with $\circ : \epsilon_{\mathbf{n}} = 0$, $\bullet : \epsilon_{\mathbf{n}} = -1$. The three curves correspond to the perfect waveguide, the double quantum well with averaged interface roughness, and the full perturbation (top to bottom).

distribution of the defects at the interfaces, are specified in the inset of Fig. 3. For comparison, we show also the conductance of the perfect quantum wire as well as the conductance in the "virtual crystal" approximation. The latter is obtained by averaging over the interface roughness, i.e., by replacing the actual potential values $\epsilon_{n_x n_y}$ by

$$\bar{\epsilon}_{n_x n_y} = \frac{1}{N_y} \sum_{n_y'=1}^{N_y} \epsilon_{n_x n_y'}, \qquad n_y = 1, \ldots, N_y, \quad (34)$$

which is independent of n_y. As may be expected, we find that defects lead always to an increase of the resistance, irrespective of their local distribution. This holds also for the perturbation $\bar{\epsilon}_{n_x n_y}$, even though it does not break the vertical symmetry of the wire and, thus, does not couple between the propagating modes of the waveguide. The conductance of the unperturbed perfect waveguide is described by Eq. (18). The steps correspond to changes in the number of propagating modes at the respective energies. The conductance spectrum of the waveguide is, therefore, symmetric with respect to $E = 0$. This symmetry as well as the steps in the conductance are destroyed by the double quantum well. This is true already for the perturbation described by Eq. (34). In this case, each propagating mode is perturbed by the same lateral perturbation which leads to a Fabry-Pérot-like transmission spectrum. The resulting conductance at energy E is obtained from the superposition of the individual contributions of the different propagating channels ν, which are identical besides a shift in energy by $E_\nu^{(y)}$ [see Eqs. (9) and (10)]. The asymmetry of the transmission probability with respect to $E = 0$ results from the fact that the considered perturbation is attractive on the average, which shifts the spectrum to lower energy.

The lowest curve in Fig. 3 shows the conductance for the double quantum well in presence of interface roughness. We find that the vertical disorder leads again to a further general increase of the resistance. At certain energies, however, the resistance may even decrease. The most striking consequence of the vertical disorder is the appearance of rather sharp resonance structures in the conductance spectrum, which correspond to fluctuations of the order of e^2/h. It is already clear from the previous discussion that these additional structures are due to the coupling between the modes of the waveguide and the localized states introduced by the defects, i.e., they can be understood as Fano resonances.

In order to arrive at a better understanding of the rather complicated conductance spectrum in Fig. 3, we present in the following the results for different types of defects in a double chain, which corresponds to $N_y = 2$. In Fig. 4, we show the transmission spectrum in the symmetric channel for the simplest possible case of a single impurity. The parameters describing the defect are $\sigma_0 = 1$ and $\alpha_0 = 0.2$ [see Eq. (30)]. The energy dependence can be easily understood in terms of Eqs. (31) and (33): The transmission is reduced by the symmetric part of the perturbation σ_0; the antisymmetric part α_0 leads to a pronounced Fano resonance. In agreement with our previous theoretical analysis, the transmission vanishes at precisely the energetic position of the localized impurity level which is obtained by evaluating Eq. (27) for the antisymmetric band. Similar results are obtained for other parameters: The overall transmission decreases with increasing σ_0; the Fano resonance broadens with increasing α_0 and it shifts to lower energy for increasing σ_0. These findings are in agreement with those of of Tekman and Bagwell,[18] who used a two-mode approximation.

The importance of the coupling between localized states and propagating waveguide modes is revealed by the local current distribution shown in Fig. 5. At energies far from the resonance, the current flow is homogeneous over the sample. Approaching the resonance, however, we find a strongly inhomogeneous current distribution in the defect region. The local vortexlike current, which is found for energies close to the transmission zero at $E \cong -1.24$, becomes even an order of magnitude larger

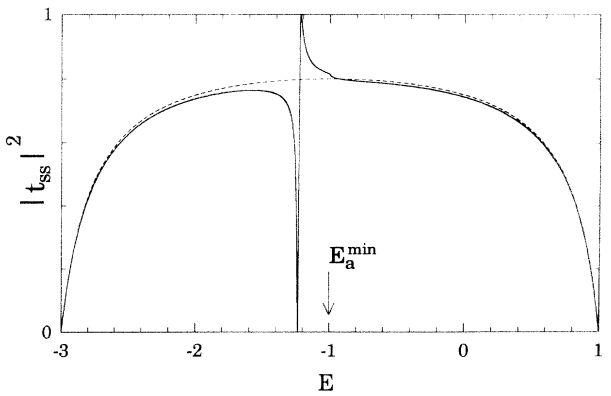

FIG. 4. Transmission probability in the symmetric channel for the Anderson double chain containing one impurity with $\sigma = 1$, $\alpha = 0.2$. The broken line gives the result for $\alpha = 0$.

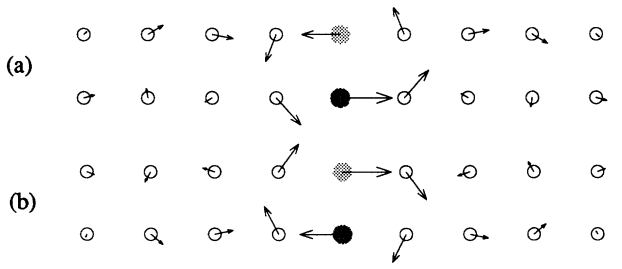

FIG. 5. Local current distribution for the Anderson double chain containing one impurity (same potential parameters as in Fig. 4) at energies E near the Fano resonance (see Fig. 4); (a) $E = -1.25$; (b) $E = -1.23$.

than the average homogeneous current observed far from the defects.[23] The sense of rotation of the local current is reversed when passing the energy of the localized resonant level. This behavior gives clear evidence for the important contribution of the impurity state to the wave function, which is given by the superposition of traveling waves and the localized wave function of the impurity state.

We now consider the case of two defects separated by a perfect waveguide and located at the positions l and r. The distance between the defects is $d = (l-r)a$. For simplicity, we present the results for identical defects with $\sigma_l = \sigma_r \equiv \sigma = 1$ and $\alpha_l = \alpha_r \equiv \alpha = 0.2$. Figure 6 shows the transmission probability in the symmetric mode for different distances. As expected, we find two Fano resonances which are associated with the two interacting localized impurity states of Eq. (27). The splitting between the two bound states is caused by the interaction term $\mathcal{W}^{(l)}\mathcal{Z}^{(r-l)}\mathcal{W}^{(r)}$ [see Eq. (32)], which is largest for small distances and vanishes for large distances. This explains the influence of the distance on the relative position of the respective transmission minima. Note that for adjacent perturbations ($d = a$), the upper level is pushed beyond the minimum of the antisymmetric band and is, therefore, not seen in the transmission spectrum.[24] For large distances (see, e.g., the case $d = 10a$), the separation between the bound states becomes very small. Moreover, the resonance minima do not necessarily reach zero value. In the latter case, the equation for the bound state associated with the antisymmetric band $\kappa_a - \kappa_a{}^{-1} + \mathcal{U}_{aa} = 0$ (see discussion at the end of Sec. II) has no solution. It should be noted, that this situation is due to the energy dependence of $\mathcal{U}_{aa}$ and can, therefore, only occur for defects which are extended in the direction of propagation. The bound states and the corresponding zeros in the transmission are, however, recovered when the antisymmetric potential parameter α is reduced.

We further note that the two Fano resonances in Fig. 6 are oriented in the opposite sense: Depending on the distance, both resonance maxima are situated either inside or outside the energy interval defined by the transmission zeros. Figure 7 shows that for antisymmetric potentials

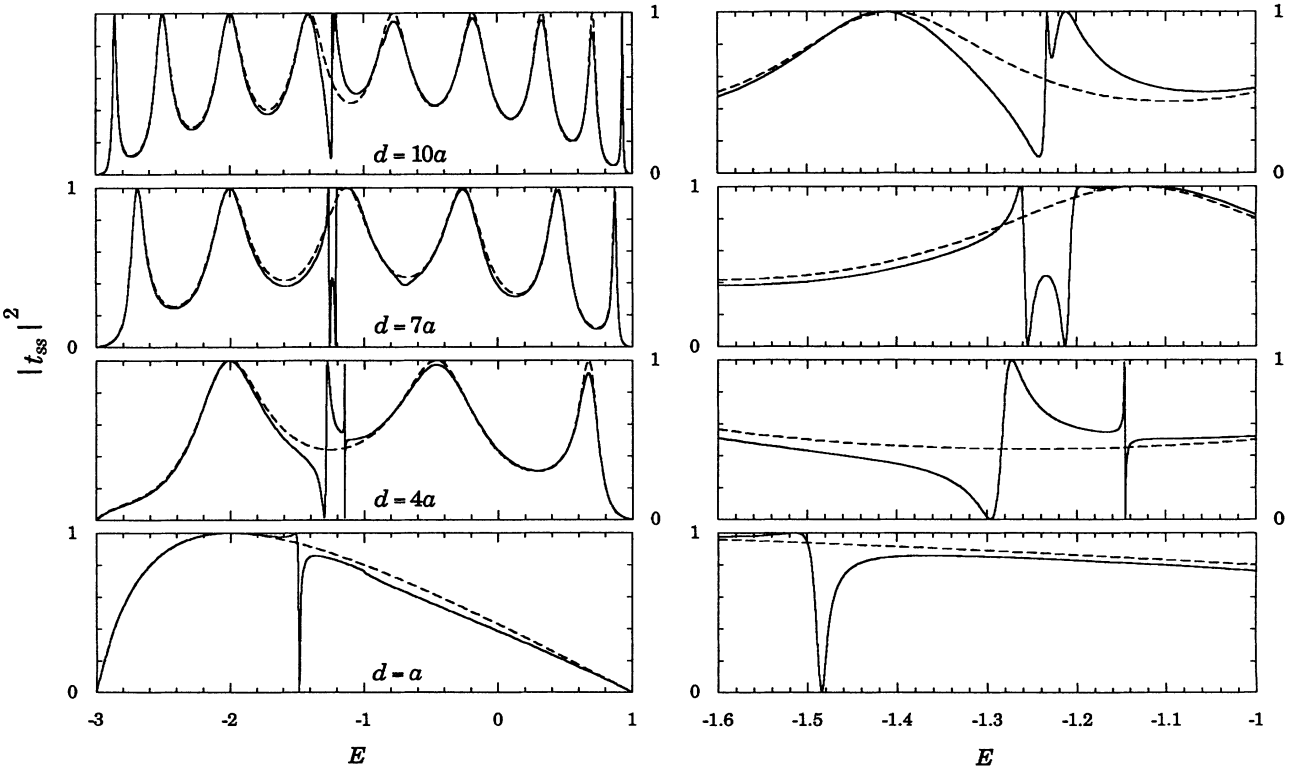

FIG. 6. Transmission probability in the symmetric channel for the Anderson double chain containing two identical perturbations with $\sigma = 1$ and $\alpha = 0.2$. The defects are separated by the distance d. To the left the results are presented over the full energy range of the symmetric channel, to the right the behavior near the Fano resonances is given with higher resolution in energy. The broken lines give the results for $\alpha = 0$.

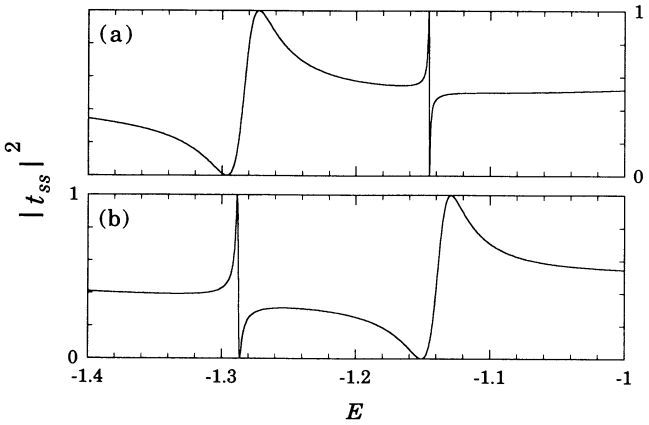

FIG. 7. Transmission probability near the resonances in the symmetric channel for the Anderson double chain containing two perturbations. The defects are separated by the distance $d = 4a$. Curve (a) shows the result for identical potentials at both positions (same parameters as in Fig. 6), curve (b) presents the result for opposite antisymmetric potentials at both positions, but the same parameters otherwise.

with opposite signs at the two sites, the relative order of minima and maxima is reversed but the opposite orientation of both resonances is maintained.

In Fig. 8, we present the current distribution for $d = 4a$ at energies close to the resonance minima. We find vortexlike behavior of the local currents near both defects. The sense of rotation of the local current changes when passing from one side of the resonance zero to the other. For identical defects [see Figs. 8(a.1) and 8(a.2)] both vortices have the same sign. They oppose each other when the antisymmetric potentials at the two defects have opposite signs [see Figs. 8(b.1) and 8(b.2)].

The dependence of the transmission spectrum on the antisymmetric-potential parameter α is shown in Fig. 9 for two identical defects at the distance $d = 11a$. The symmetrical potential for both defects is again $\sigma = 1$.

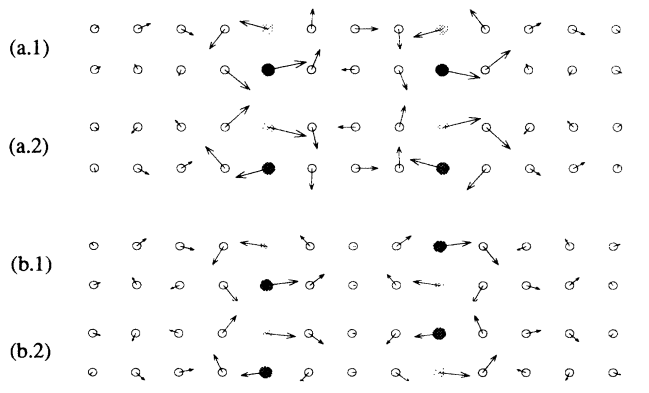

FIG. 8. Current distribution for the same configurations and potential parameters as in Fig. 7. The energies for the the cases (a.1), (a.2) and (b.1), (b.2) are chosen close to the Fano resonances seen in Figs. 7(a) and 7(b), respectively. (a.1) $E = -1.31$; (a.2) $E = -1.29$; (b.1) $E = -1.16$; (b.2) $E = -1.14$.

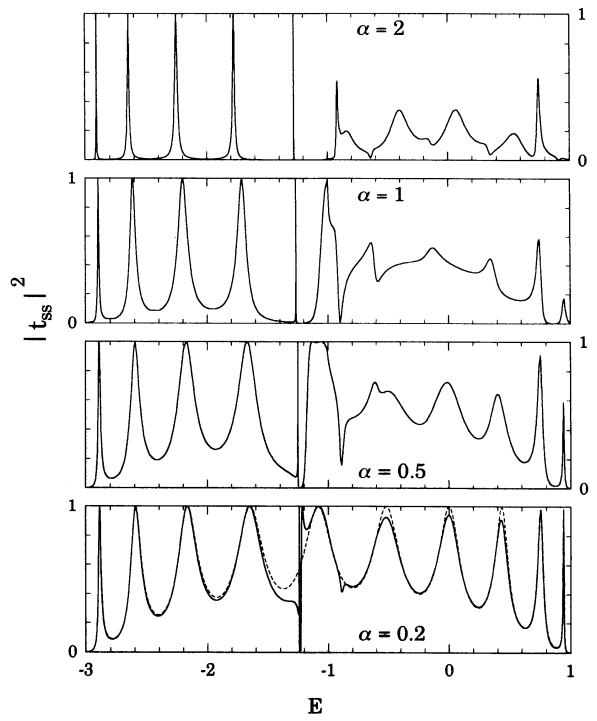

FIG. 9. Transmission spectra in the symmetric channel for the Anderson double chain containing two perturbations at the distance $d = 11a$. The symmetric part of the perturbing potentials is given by $\sigma = 1$. The results are given for different antisymmetric parameters α of the perturbing potential. In the figure, at the bottom, the Fabry-Pérot spectrum for $\alpha = 0$ is also shown (broken line).

For vanishing α we find the expected Fabry-Pérot spectrum for a 1D chain. Two distinct Fano resonances can be resolved for small values α near $E = -1.2$. Both resonances repel each other for increasing α. This can be explained by the increased effective interaction $\mathcal{U}_{sa}$ between the defect states. For $\alpha = 0.5$ the upper level merges with the Fabry-Pérot peak at $E \cong -1.1$. We also observe a drastical α dependence of the Fabry-Pérot oscillations. For energies $E < -1$, i.e., below the minimum of the antisymmetric band (see Fig. 2), the Fabry-Pérot peaks sharpen with increasing α. For energies in the range of the antisymmetric band ($-1 < E < 1$) the Fabry-Pérot oscillations are strongly damped. In this energy range, we obtain, also, additional structures in the transmission spectrum for large values α. Both effects, the damping as well as the appearance of the new structures are due to the simultaneous presence of Fabry-Pérot interferences involving both the symmetric and the antisymmetric channels, which become more and more important with increasing α. These multichannel Fabry-Pérot interferences can be easily understood. Let us first recall the conditions in the single-channel case, where only waves in the symmetric channel interfere. Considering the case of destructive interference, we obtain the relation

$$2q_s(E)d + 2\gamma_s(E) = (2n+1)\pi, \tag{35}$$

with integer n, which gives the condition for the minima

in the spectrum for $\alpha = 0$. Here, $q_s(E)$ is the wave vector in the symmetric channel at energy E, and $\gamma_s(E)$ is the phase of the reflection coefficient $s_{11} = |s_{11}| \exp[i\gamma_s(E)]$ for the individual (identical) scatterers. For large α values the waves change their symmetry after each reflection, and we are, therefore, left with the condition for destructive *two-channel* Fabry-Pérot interference,

$$[q_s(E) + q_a(E)]\, d + \gamma_s(E) + \gamma_a(E) = (2n+1)\,\pi, \quad (36)$$

where $q_a(E)$ $[\gamma_a(E)]$ is the wave vector (phase of the reflection coefficient) in the antisymmetric channel at energy E. At intermediate α values incoming waves of either symmetry are reflected into both channels, and the two paths interfere with each other, thus leading to a damping of the Fabry-Pérot oscillations of $|t_{ss}|^2$. For large α, the two-channel mechanism described by Eq. (36) dominates. This gives rise to the additional structures in Fig. 9, which are particularly well resolved near the edge of the antisymmetric band. It should be noted, that the physics underlying the Fabry-Pérot oscillations and the Fano resonances is rather the same, and that the above description in terms of Fabry-Pérot interferences is only chosen for reasons of tradition. In fact, the situation could equally well be described in the Fano picture, which relates the structures in the transmission spectra to the coupling between quasibound levels and the continuum of propagating states. For this, one has simply to recognize that multiple reflections between the two defects give rise to a quasibound state, provided that the reflection coefficients are sufficiently large. Here again, it is easy to verify that the energies of the quasibound states correspond to the *minima* (and not to the maxima, as is often assumed) in the Fabry-Pérot transmission or conductance spectra.

The transmission spectrum for the symmetric mode in a single quantum well with symmetry breaking defects at the interfaces is given in Fig. 10. The slow oscillations are due to Fabry-Pérot interferences in the symmetric channel, which correspond to the scattering between both interfaces. Interchannel coupling due to the disorder at the interfaces gives rise to two typical Fano resonances positioned at the bound eigenstates of the well for the antisymmetric band, which can be calculated from Eq. (27). We note that the vertical disorder at the interfaces is rather large, which explains its strong influence on the whole spectrum. The width of the resonance decreases with the binding energy. This corresponds to the decreasing amplitude of the localized wave function in the region of the interfaces. Moreover, Fig. 10 shows that already for $\alpha_{n_x} = 0$, i.e., without interchannel coupling, the transmission is almost suppressed for $E > 0$. This is a band-structure effect: For sufficiently large wells one may define a local band structure in the well which is shifted to lower energies by the amount of the attractive well potential. With this alignment of bands, energies near the upper edge of band s correspond to evanescent states in the well region, i.e., incoming waves in this energy range are reflected by the well. The low-energy edge of the spectrum is not shifted, since it is defined by the propagating states of the unperturbed quantum guide.

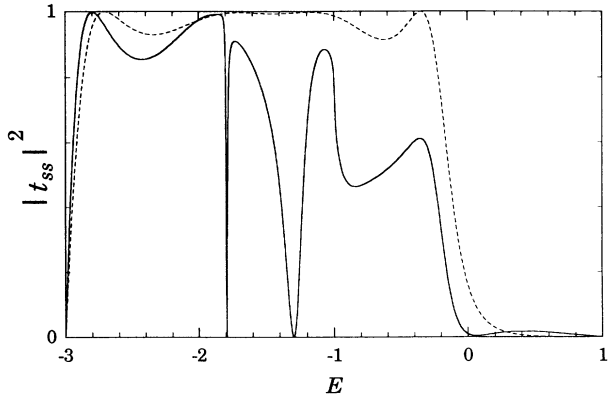

FIG. 10. Transmission probability in the symmetric channel for the Anderson double chain in presence of a perturbed single quantum well. The perturbed well extends over the distance $d = 5a$. The left (right) interface is described by the potential parameters $\sigma_l = 0.66$, $\alpha_l = 0.5$ ($\sigma_r = 0.5$, $\alpha_r = 0.5$). The potential inside the well is given by $\sigma_{n_x} = 1$, $\alpha_{n_x} = 0$. For comparison, the Fabry-Pérot spectrum for $\alpha_l = \alpha_r = 0$ is also shown (broken line).

The same band-structure effect is also responsible for the strong dependence of the Fabry-Pérot oscillations on the energy seen in Fig. 10: At intermediate energies the oscillations are rather weak, and they become more pronounced near the edges of the transmission window. In order to understand this behavior, one has simply to recognize that near the band edges the wave vector changes rapidly with energy, thus leading to rather rapid changes of the Fabry-Pérot transmission probability in this range [see Eq. (35)]. This energy dependence is also seen in Figs. 6 and 9.

The different situations, which we have studied for the simple case of a double Anderson chain, provide a tool box for the understanding of the conductance spectra of more complex systems. To demonstrate this, we discuss again the representative case of Fig. 3, which shows the calculated conductance spectrum for a double quantum well with rough interfaces. In order to facilitate the comparison, we have chosen approximately the same wells as in Fig. 10. First of all, we observe that in presence of the well potentials the conductance spectrum becomes asymmetric with respect to $E = 0$. The conductance is strongly reduced for $E > 0$, and is even suppressed for $E > 3.4$. This behavior is readily explained by the shift of the local band structure in the well region (see the above discussion of Fig. 10). Already for the case of the averaged perturbation $\bar{\epsilon}_{n_x n_y}$, we find that the conductance fluctuations are qualitatively different for $E < 0$ and $E > 0$: The oscillations in the lower half of the spectrum are much smoother than those in the upper part. This again can be understood together with the result presented in Fig. 10. As mentioned before, the conductance spectrum is given by the sum over the contributions of the different channels, which have the typical asymmetric form presented in Fig. 10 and which are identical besides a shift in energy by $E_\nu^{(y)}$ [Eq. (9)].

The comparison of the final spectrum in Fig. 3 with the spectrum obtained for the perturbation $\bar{\epsilon}_{n_x n_y}$ shows that the influence of the interchannel coupling, which is introduced by the interface roughness, is most important in the low-energy part of the spectrum. This is due to the fact that the well potentials are attractive, and, therefore, the bound states are located *below the band minima* of the different modes. The corresponding Fano resonances can thus only be found at energies $E < 0$. We emphasize that in spite of their ressemblence with Fano resonances, the pronounced structures in the "virtual crystal" spectrum for $E > 0$ are resulting from the superposition of the identical single-mode Fabry-Pérot spectra which are shifted in energy, i.e., these structures cannot be interpreted in terms of Fano resonances at local defect states. The single quantum well possesses two bound states (see Fig. 10) with binding energies $\Delta E_1 \cong 0.8$ and $\Delta E_2 \cong 0.3$. The double well possesses, thus, four bound states which are grouped in two doublets since the well-well interaction is rather small.[25] In agreement with our theoretical description, the doublet resonances in Fig. 3 appear precisely at the energies of the localized states of the single well, which are obtained by subtracting the above binding energies from the lower band edges $E_\nu^{\min} = E_\nu^{(y)} + 2V$. Similar to Fig. 10, the width of the resonances in the conductance spectrum decreases with increasing binding energy. Moreover, the doublet splitting is largest for the less bound state.[26] This corresponds to the fact that the interwell interaction becomes negligible, when the interacting states are strongly localized within a single well.

The resonance structure consisting of two doublets is essentially repeated at each of the lower band edges of the higher modes which correspond to larger $E_\nu^{(y)}$. The replica are, however, not perfect. The deviations can be attributed to multimode mixing involving more than two channels. In fact, for $-4 < E < 0$ the number of channels which contribute to the conductance [see Eq. (20)] increases with the energy. The Fano resonances at higher energy correspond, therefore, to the interaction between a localized level and *several* propagating modes. We note that multichannel interactions will be more important for three-dimensional quantum wires, where the number of degenerate channels is increased.

In the considered case of a double well the average potential $\bar{\epsilon}_{n_x n_y}$ does not lead to bound states at energies $E > 0$. The sharp resonance peaks at energies $E \cong 2.0, 2.8$, and 3.4 in Fig. 3 can, therefore, not be attributed to Fano resonances at localized single-mode defect states, but they are due to the *multichannel* Fabry-Pérot interferences which were discussed together with Fig. 9.

IV. CONCLUSIONS

We have presented a theoretical and numerical study of the role of defects for the dc transport in multichannel quantum wires. Following the approach of Landauer, we have calculated the scattering properties of the perturbed quantum wires which determine the electronic transport, by direct solution of the Schrödinger equation for scattering boundary conditions. In this way, we do not only obtain an efficient numerical scheme, but we get also a theoretically appealing description of coherent transport in presence of defects, which offers the necessary tools for the interpretation of conductance-spectroscopy experiments. In particular, we have been able to clarify the different roles of defect-induced intrachannel coupling, which is caused by perturbations breaking the translational symmetry along the wire, and of interchannel coupling, which is due to disorder across the wire. Intrachannel coupling is responsible for Fabry-Pérot interferences in the transmission spectra of the different channels. It further introduces localized defect states which are associated with the different bands of the unperturbed quantum wire. In presence of interchannel coupling, these defect states give rise to Fano-resonance structures in the conductance spectra. It should be noted that the above general description is not restricted to any special kind of defects or defect distributions. In particular, the conductance spectra of geometrically distorted quantum wires show similar behavior[12,13] and can be understood along the same lines.

The resonances are the result of the coherent mixing between localized defect states and propagating waveguide modes. The local character of the interaction has been visualized by the local-current distributions, which are vortexlike near the defects and at energies close to the resonances. It is quite straightforward to speculate that these vortexlike local currents will become particularly important in the ac regime, where they will give rise to inductive behavior. Our results show that the basic features of the conductance spectra in multichannel quantum wires can already be understood in the simple case of the double Anderson chain. Different kinds of defects have been investigated in detail for this two-channel system. In particular, we have shown that the interaction between defects, which are spatially seaparated in the transport direction, gives rise to correlated resonance structures in the conductance spectrum. Moreover, for large interchannel coupling, we have found resonances in the transmission or conductance spectra, which can be described as multimode Fabry-Pérot interferences. Alternatively, they could also be understood as Fano resonances involving localized states which are built up from more than one band.

We note that the Fano resonances correspond always to oscillations of the order e^2/h, which is the order of the universal conductance fluctuations.[1,8–10] While this is not so surprising in itself, since the systems considered in the theory of the universal conductance fluctuations are rather the same, we may take this as an indication that the present approach may also be useful to elucidate the interference processes which are responsible for the existence of these fluctuations.

ACKNOWLEDGMENTS

This work was supported by the Swiss National Science Foundation under Grant No. 20-33452.92.

APPENDIX A: MATRIX REPRESENTATION OF THE SCHRÖDINGER EQUATION

Multiplication of Eq. (7) by $\phi^{\nu'}_{n_y n_z}$ and summation over n_y, n_z yields

$$V \sum_{n_y,n_z} \sum_{n'_y,n'_z} \phi^{\nu}_{n_y n_z} \phi^{\nu'}_{n'_y n'_z} \Delta^{(yz)}_{\mathbf{n}\mathbf{n}'} = \delta_{\nu\nu'} \left[E - V \left(\kappa_\nu + \frac{1}{\kappa_\nu} \right) \right]. \tag{A1}$$

Our aim is to write Eq. (3) in the basis of the functions $|n_x, \nu, E\rangle$. We, therefore, calculate the matrix elements

$$\begin{aligned} \langle n_x, \nu, E|H - E|n'_x, \nu', E\rangle &= (\kappa^*_\nu)^{n_x} (\kappa_{\nu'})^{n'_x} \sum_{n_y,n_z} \sum_{n'_y,n'_z} \phi^{\nu}_{n_y n_z} \phi^{\nu'}_{n'_y n'_z} \left[V \left(\Delta^{(x)}_{\mathbf{n}\mathbf{n}'} + \delta_{n_x n'_x} \Delta^{(yz)}_{\mathbf{n}\mathbf{n}'} \right) + (\epsilon_{\mathbf{n}} - E)\, \delta_{\mathbf{n}\mathbf{n}'} \right] \\ &= V \delta_{\nu\nu'} |\kappa_\nu|^{2n_x} \left(\kappa_\nu \left(\delta_{n_x n'_x - 1} - \delta_{n_x n'_x} \right) + \frac{1}{\kappa_\nu} \left(\delta_{n_x n'_x + 1} - \delta_{n_x n'_x} \right) \right) + V \delta_{n_x n'_x} |\kappa_\nu|^{2n_x} \mathcal{W}^{(n_x)}_{\nu\nu'}, \end{aligned} \tag{A2}$$

where we have used Eq. (A1). $\mathcal{W}^{(n_x)}$ is defined by Eq. (16). The Hamiltonian Eq. (4) contains only couplings between nearest neighbors. It follows that only matrix elements involving layers with $n_x^{\bar{M}} = \{l-1, \ldots, r+1\}$ contribute to the defect-induced interaction between the states of the perfect waveguide. From Eq. (A2), we obtain for $n_x \in \bar{M}$,

$$\begin{aligned} \langle n_x, \nu, E|H - E|\bar{\nu}\rangle/V &= |\kappa_\nu|^{2n_x} \left(-\delta_{n_x,l-1} \kappa_\nu + \delta_{n_x,l} \frac{1}{\kappa_\nu} \right) \delta_{\nu\bar{\nu}}, \\ \langle n_x, \nu, E|H - E|\psi^{(L)}_{\bar{\nu}}\rangle/V &= |\kappa_\nu|^{2n_x} \kappa_\nu^{-2n_x} \left(-\delta_{n_x,l-1} \frac{1}{\kappa_\nu} + \delta_{n_x,l} \kappa_\nu \right) \xi_{\nu\bar{\nu}}, \\ \langle n_x, \nu, E|H - E|\psi^{(M)}_{\bar{\nu}}\rangle/V &= |\kappa_\nu|^{2n_x} (1 - \delta_{n_x,r} - \delta_{n_x,r+1})\, \kappa_\nu \psi^{\bar{\nu}}_{n_x+1,\nu} + |\kappa_\nu|^{2n_x} (1 - \delta_{n_x,l-1} - \delta_{n_x,l}) \frac{1}{\kappa_\nu} \psi^{\bar{\nu}}_{n_x-1,\nu} \\ &\quad + |\kappa_\nu|^{2n_x} (1 - \delta_{n_x,l-1} - \delta_{n_x,r+1}) \left[\sum_{\nu'} \mathcal{W}^{(n_x)}_{\nu\nu'} \psi^{\bar{\nu}}_{n_x\nu'} - \left(\kappa_\nu + \frac{1}{\kappa_\nu} \right) \psi^{\bar{\nu}}_{n_x\nu} \right], \\ \langle n_x, \nu, E|H - E|\psi^{(R)}_{\bar{\nu}}\rangle/V &= |\kappa_\nu|^{2n_x} \left(\delta_{n_x,r} \kappa_\nu - \delta_{n_x,r+1} \frac{1}{\kappa_\nu} \right) \xi_{\nu+N,\bar{\nu}}. \end{aligned} \tag{A3}$$

With the above matrix elements and Eqs. (11) and (12), we can write Eq. (3) in the basis of the functions $|n_x, \nu, E\rangle$ and obtain Eq. (14).

APPENDIX B: RECURSION RELATION FOR TRANSFER MATRICES

In the following, we prove Eq. (22). Its validity for $i = 0$ follows immediately from the definition Eq. (21) and the last line of the Schrödinger equation Eq. (14). It holds also for $i = 1$, since with Eq. (23), we have $\mathcal{Z}^{(1)} = \mathcal{K}$: which satisfies the next to last line of the Schrödinger equation. The following lines of Eq. (14) read for $2 \le i \le r - l$:

$$\Psi^{(r-i)} = -\mathcal{K} \left(\mathcal{K} \Psi^{(r-i+2)} + \mathcal{M}^{(r-i+1)} \Psi^{(r-i+1)} \right), \tag{B1}$$

which gives together with Eq. (21),

$$\mathcal{T}^{(i)} = -\mathcal{K} \left(\mathcal{K} \mathcal{T}^{(i-2)} + \mathcal{M}^{(r-i+1)} \mathcal{T}^{(i-1)} \right). \tag{B2}$$

We now assume that Eq. (22) is valid for $\mathcal{T}^{(i-2)}$ and $\mathcal{T}^{(i-1)}$, and prove that it is also true for the subsequent transfer matrix $\mathcal{T}^{(i)}$. Expressing $\mathcal{M}^{(r-i+1)}$ by Eq. (15), we obtain

$$\begin{aligned} \mathcal{T}^{(i)} &= -\mathcal{K}^2 \left(\mathbf{1} - \sum_{j=1}^{i-2} \mathcal{Z}^{(j)} \mathcal{W}^{(r-i+j+2)} \mathcal{T}^{(i-j-2)} \right) - \mathcal{K} \left(\mathcal{W}^{(r-i+1)} - \mathcal{K} - \mathcal{K}^{-1} \right) \left(\mathbf{1} - \sum_{j=1}^{i-1} \mathcal{Z}^{(j)} \mathcal{W}^{(r-i+j+1)} \mathcal{T}^{(i-j-1)} \right) \\ &= \mathbf{1} - \mathcal{K} \mathcal{W}^{(r-i+1)} \mathcal{T}^{(i-1)} - \left(\mathcal{K}^2 + \mathbf{1} \right) \mathcal{Z}^{(1)} \mathcal{W}^{(r-i+2)} \mathcal{T}^{(i-2)} - \sum_{j=3}^{i} \left[\left(\mathcal{K}^2 + \mathbf{1} \right) \mathcal{Z}^{(j-1)} - \mathcal{K}^2 \mathcal{Z}^{(j-2)} \right] \mathcal{W}^{(r-i+j)} \mathcal{T}^{(i-j)}. \end{aligned} \tag{B3}$$

From Eq. (23) it follows that the expression in the square brackets in Eq. (B3) equals $\mathcal{Z}^{(j)}$ and $\left(\mathcal{K}^2 + \mathbf{1} \right) \mathcal{Z}^{(1)} = \mathcal{Z}^{(2)}$, and we obtain Eq. (22).

APPENDIX C: DIRECT CALCULATION OF THE TRANSMISSION COEFFICIENTS

From Eq. (14), we obtain for the inhomogeneous linear equations corresponding to the layers $n_x = l-1$ and l,

$$\mathcal{K}^{-2l+1}\mathbf{X}^{(L)} = \mathcal{K}\Psi^{(l)} - \mathcal{K}, \tag{C1}$$

$$\mathcal{K}^{-2l+1}\mathbf{X}^{(L)} = -\mathcal{M}^{(l)}\Psi^{(l)} - \mathcal{K}\Psi^{(l+1)} - \mathcal{K}^{-1}. \tag{C2}$$

We note that Eq. (C1) together with Eq. (21) relates the left- and right-hand solutions $\mathbf{X}^{(L)}$ and $\mathbf{X}^{(R)}$ by

$$\mathbf{1} + \mathcal{K}^{-2l}\mathbf{X}^{(L)} = \mathcal{T}^{(r-l)}\mathbf{X}^{(R)}. \tag{C3}$$

Using Eqs. (C3), (21), and (15), Eq. (C2) becomes

$$\left[\left(\mathcal{W}^{(l)} - \mathcal{K}^{-1}\right)\mathcal{T}^{(r-l)} + \mathcal{K}\mathcal{T}^{(r-l-1)}\right]\mathbf{X}^{(R)} = \mathcal{K} - \mathcal{K}^{-1}. \tag{C4}$$

In order to show the equivalence of Eqs. (C4) and (24), we have to show that

$$\left(\mathcal{W}^{(l)} - \mathcal{K}^{-1}\right)\mathcal{T}^{(r-l)} + \mathcal{K}\mathcal{T}^{(r-l-1)} = \mathcal{K} - \mathcal{K}^{-1} + \sum_{j=l}^{r}\mathcal{W}^{(j)}\mathcal{T}^{(r-j)}, \tag{C5}$$

where we have already expressed $\mathcal{U}$ by Eq. (25). Using the recursion relation Eq. (22), we obtain

$$\begin{aligned}\left(\mathcal{W}^{(l)} - \mathcal{K}^{-1}\right)\left(\mathbf{1} - \sum_{j=1}^{r-l}\mathcal{Z}^{(j)}\mathcal{W}^{(l+j)}\mathcal{T}^{(r-l-j)}\right) + \mathcal{K}\left(\mathbf{1} - \sum_{j=1}^{r-l-1}\mathcal{Z}^{(j)}\mathcal{W}^{(l+j+1)}\mathcal{T}^{(r-l-j-1)}\right)&\\ = \mathcal{K} - \mathcal{K}^{-1} + \mathcal{W}^{(l)}\mathcal{T}^{(r-l)} + \mathcal{K}^{-1}\sum_{j=l+1}^{r}\mathcal{Z}^{(j-l)}\mathcal{W}^{(j)}\mathcal{T}^{(r-j)} - \mathcal{K}\sum_{j=l+2}^{r}\mathcal{Z}^{(j-l-1)}\mathcal{W}^{(j)}\mathcal{T}^{(r-j)}&\\ = \mathcal{K} - \mathcal{K}^{-1} + \sum_{j=l}^{l+1}\mathcal{W}^{(j)}\mathcal{T}^{(r-j)} + \sum_{j=l+2}^{r}\left[\mathcal{K}^{-1}\mathcal{Z}^{(j-l)} - \mathcal{K}\mathcal{Z}^{(j-l-1)}\right]\mathcal{W}^{(j)}\mathcal{T}^{(r-j)}.&\end{aligned} \tag{C6}$$

From Eq. (23) we obtain $[\cdots] = \mathbf{1}$. Inserting this in Eq. (C6), we obtain Eq. (C5).

[1] For an overview see, e.g., *Quantum Coherence in Mesoscopic Systems*, edited by B. Kramer (Plenum, New York, 1991).

[2] R. Landauer, IBM J. Res. Dev. **1**, 223 (1957); Philos. Mag. **21**, 863 (1970).

[3] R. Landauer, Z. Phys. B **68**, 217 (1987); J. Phys. Condens. Matter **1**, 8099 (1989).

[4] A. MacKinnon and B. Kramer, Z. Phys. B **53**, 1 (1981); B. Kramer and M. Schreiber, in *Fluctuations and Stochastic Phenomena in Condensed Matter*, edited by L. Garrido, Lecture Notes in Physics Vol. 268 (Springer, Berlin, 1987), p. 351.

[5] See, e.g., P. A. Lee and T. V. Ramakrishnan, Rev. Mod. Phys. **57**, 287 (1985), and references therein.

[6] M. Büttiker, Y. Imry, and R. Landauer, Phys. Rev. Lett. **52**, 129 (1983); M. Büttiker, *ibid.* **57**, 1761 (1986); M. Büttiker, Y. Imry, R. Landauer, and S. Pinkas, Phys. Rev. B **31**, 6207 (1985).

[7] F. Gagel and K. Maschke, Phys. Rev. B **49**, 17 170 (1994).

[8] C. P. Umbach, S. Washburn, R. B. Laibowitz, and R. A. Webb, Phys. Rev. B **30**, 4048 (1984).

[9] R. A. Webb, S. Washburn, C. P. Umbach, and R. A. Laibowitz, Phys. Rev. Lett. **54**, 2696 (1985).

[10] A. D. Stone, Phys. Rev. Lett. **54**, 2692 (1985); P. A. Lee and A. D. Stone, *ibid.* **55**, 1622 (1985); A. D. Stone, in *Physics and Technology of Submicron Structures*, edited by H. Heinrich, G. Bauer, and F. Kuchar, Springer Series in Solid-State Sciences Vol. 83 (Springer, Berlin, 1988), pp. 108–127.

[11] S. K. Kirby, D. Z.-Y. Ting, and T. C. McGill, Phys. Rev. B **48**, 15 237 (1993).

[12] T. Kawamura and J. P. Leburton, Phys. Rev. B **48**, 8857 (1993).

[13] K.-F. Berggren, C. Besev, and Zhen-Li Ji, Phys. Scr. **T42**, 141 (1992).

[14] Y. Takagaki and K. Ploog, Phys. Rev. B **48**, 11 508 (1993).

[15] J. L. D'Amato and H. M. Pastawski, Phys. Rev. B **41**, 7411 (1990).

[16] M. Büttiker, Phys. Rev. B **33**, 3020 (1986).

[17] K. Maschke and M. Schreiber, Phys. Rev. B **44**, 3835 (1991); **49**, 2295 (1994).

[18] E. Tekman and P. F. Bagwell, Phys. Rev. B **48**, 2553

(1993).
[19] W. Porod, Zhi-an Shao, and C. S. Lent, Phys. Rev. B **48**, 8495 (1993); Ch. Kunze, *ibid.* **48**, 14 338 (1993); Zhi-an Shao, W. Porod, and C. S. Lent, *ibid.* **49**, 7453 (1994).
[20] T. B. Boykin, Phys. Rev. B **47**, 12 696 (1993).
[21] In principle, the waveguide Hamiltonian H_0 is also separable with respect to the coordinates y and z. This fact is, however, not important for our general discussion. It remains of course useful for the solution of Eq. (9).
[22] D. S. Fisher and P. A. Lee, Phys. Rev. B **23**, 6851 (1981).
[23] The existence of current vortices in perturbed quantum wires has already been discussed by S. Chaudhuri, S. Bandyopadhyay, and M. Cahay, Phys. Rev. B **47**, 12 649 (1993).
[24] A similar case has been discussed by A. Kumar and P. F. Bagwell, Phys. Rev. B **43**, 9012 (1991).
[25] In the considered case, the average potentials $\bar{\epsilon}_{n_x n_y}$ at the interfaces are not exactly the same, which gives rise to an additional small contribution to the splitting.
[26] Note that the structure at $E \cong -3.6$ ($E \cong -3.25$) corresponds to the weakly (strongly) bound state associated with the second (third) band, which has its minimum at $E \cong -3.24$ ($E \cong -3.45$).

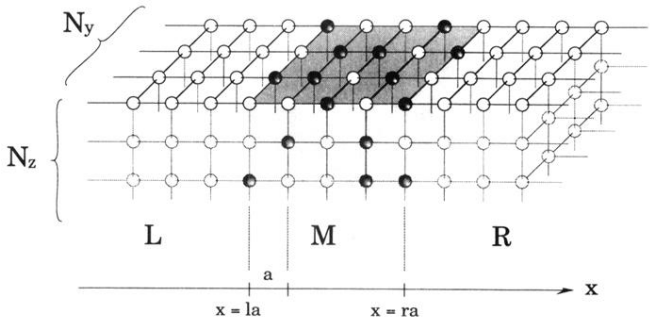

FIG. 1. Quantum wire with defects in the Anderson model. L and R denote the regions of the semi-infinite waveguides, which are connected to electron reservoirs with different chemical potentials. The region M contains the defects.

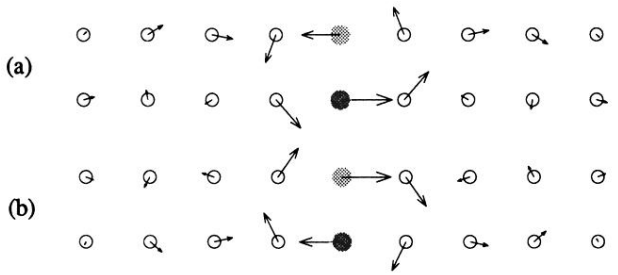

FIG. 5. Local current distribution for the Anderson double chain containing one impurity (same potential parameters as in Fig. 4) at energies E near the Fano resonance (see Fig. 4); (a) $E = -1.25$; (b) $E = -1.23$.

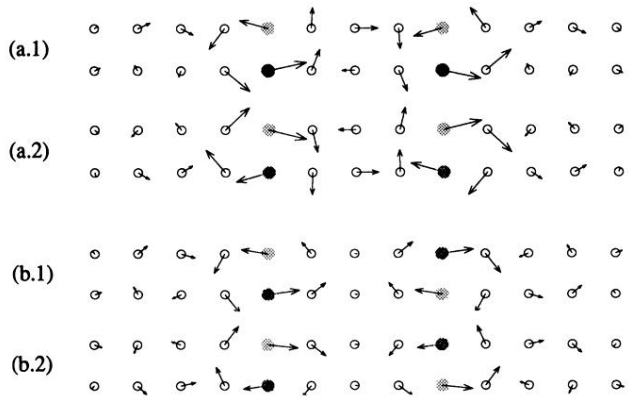

FIG. 8. Current distribution for the same configurations and potential parameters as in Fig. 7. The energies for the the cases (a.1), (a.2) and (b.1), (b.2) are chosen close to the Fano resonances seen in Figs. 7(a) and 7(b), respectively. (a.1) $E = -1.31$; (a.2) $E = -1.29$; (b.1) $E = -1.16$; (b.2) $E = -1.14$.